ORIGINAL PAPER

A cobalt oxide@polydopamine-reduced graphene oxide-based 3D photothermal evaporator for highly efficient solar steam generation

Ting Gao[1] · Xuan Wu[1] · Gary Owens[1] · Hao-Lan Xu[1]

Abstract

Improving the evaporation rate and energy efficiency of solar steam generation is very important to facilitate real-world applications for clean water production. In this work, Co_3O_4@polydopamine (PDA) nanoparticles were synthesized and combined with reduced graphene oxide (rGO) to fabricate a new Co_3O_4@PDA-rGO photothermal aerogel. The obtained photothermal aerogel sheet was thereafter used to prepare both two-dimensional (2D) and three-dimensional (3D) photothermal evaporators for solar steam generation. Due to the excellent light absorption and hydrophilicity of the photothermal aerogel, a high evaporation rate of 1.60 kg·m^{-2}·h^{-1} was achieved for the 2D photothermal evaporator. While for the 3D evaporator, the evaporation rate was dramatically increased to 3.71 kg·m^{-2}·h^{-1} with a corresponding light-to-vapor energy efficiency of 107%. This was attributed to an increased evaporation surface area, decreased energy loss from the top evaporation surface to the environment, and energy gain from the environment on the side evaporation surface. The 3D evaporator also showed excellent practical performance in seawater desalination thus demonstrating great potential for real-world applications.

Keywords Solar-steam generation · Cobalt oxide · Polydopamine · Reduced graphene oxide · Photothermal materials · Seawater desalination

1 Introduction

Interfacial solar steam generation (ISSG) is a promising technology for various applications including solar energy conversion, seawater desalination, wastewater purification, sterilization, electricity generation, and hydrogen production [1–10]. ISSG is recognized as a green and cost-effective approach for clean water supply, because it harvests and converts the clean, renewable, and abundant solar energy into thermal energy to drive water evaporation [11, 12]. Compared to traditional solar-thermal bulk water heating systems, ISSG is able to localize converted heat at air–water interfaces for water evaporation, thus delivering superior energy efficiencies [13–15]. However, to facilitate future

real-world applications, the evaporation rate and energy efficiency of ISSG still need to be improved to obtain higher clean water output. To achieve this, the development of high-performance photothermal materials (PTMs) for efficient light-to-heat conversion and rational design of the structure of photothermal evaporator to optimize energy management during solar steam generation are prerequisite [16]. For ISSG, applied PTMs can be classified into four main categories including carbon-based materials [16–27], metallic plasmonic materials [28–33], polymers [34–36], and semiconductors [37–39]. Among the semiconductors, metal oxides and chalcogenides such as Cu_xS_y, $Cu_{12}Sb_4S_{13}$, Fe_3O_4, CuO, MoO_{3-x}, and TiO_x, have the advantages of low-toxicity, relative mild synthetic conditions, and high light absorption [37, 39–44]. These semiconductors have shown excellent performance when used as PTMs in ISSG. Co_3O_4 is also an excellent photothermal semiconductor routinely used in concentrated solar power systems [45], where its outstanding thermal stability allows it to function at high temperatures > 750 °C. However, such a promising PTM candidate has rarely been applied for ISSG [46, 47].

Apart from PTM optimization, the rational design of the structure/configuration of the photothermal evaporator also

✉ Hao-Lan Xu
  haolan.xu@unisa.edu.au

1 Future Industries Institute, University of South Australia, Adelaide, SA 5095, Australia

significantly contributes to enhancing solar evaporation via minimizing energy loss and maximizing energy input [16, 17, 19, 33, 48–51]. For example, one-dimensional (1D) or two-dimensional (2D) water path has been introduced between the PTMs (i.e., evaporation surfaces) and the bulk water to spatially separate these two parts, and thus minimizes the conductive heat loss from the evaporation surface to the bulk water, remarkably improving the overall energy efficiency of solar evaporation [34, 39, 52–54]. Three-dimensional (3D) evaporators composed of both a solar evaporation surface and a cold evaporation surface have also been fabricated, in which the cold evaporation surface is able to harvest additional energy from the surrounding air to support solar evaporation [19, 49–51, 55]. In addition, some elaborately designed 3D evaporators have also been shown to have the ability to recycle latent heat from vapor condensation [16, 56, 57] and extract energy from the bulk water during solar steam generation to enhance solar evaporation [58]. These merits have rendered the 3D evaporators extremely high evaporation rates and energy efficiencies even beyond the theoretical light-to-vapor conversion limit.

In this work, Co_3O_4 nanoparticles (NPs) were synthesized and incorporated with polydopamine (PDA) and reduced graphene oxide (rGO) to fabricate 2D and 3D photothermal evaporators for solar steam generation. Co_3O_4 is a typical p-type semiconductor with excellent light absorption across the ultraviolet–visible (UV–Vis) regions [45]. PDA, a well-known photothermal polymer which can grow on any substrates by self-polymerization, was coated on the Co_3O_4 NP surface (Co_3O_4@PDA) to enhance hydrophilicity [33, 34, 59, 60]. Commercial rGO nanosheets were introduced to compensate the light absorption in the near-infrared (NIR) region, thus endowing the hybrid PTM (Co_3O_4@PDA-rGO) with excellent light absorption across the UV–Vis–NIR regions. The obtained Co_3O_4@PDA-rGO-based 3D photothermal evaporator integrated with an oil lamp-like evaporation setup (Fig. 1) showed the ability to harvest energy not only from the incident light, but also from the surrounding environment, thus delivering an extremely high evaporation rate.

2 Experimental

2.1 Chemicals and materials

Cobalt chloride ($CoCl_2 \cdot 6H_2O$), sodium hydroxide (NaOH), hydrochloride acid (HCl), dopamine hydrochloride, $CuSO_4 \cdot 5H_2O$, H_2O_2, ethanol, urea, and agarose were purchased from Sigma-Aldrich, Australia. Commercial rGO was provided by Huasheng Graphite Co., Ltd, China. Commercial cellulose–cotton sheets containing 70% cellulose and 30% cotton were purchased from a local market.
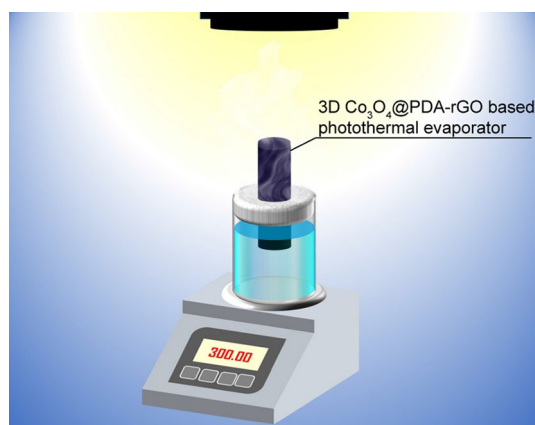

Fig. 1 Schematic illustration of the oil lamp-like solar evaporation system using a 3D Co_3O_4@PDA-rGO photothermal evaporator

Unless otherwise noted, Milli-Q (MQ) water with a resistance > 18.2 MΩ·cm^{-1} was used for all experiments.

2.2 Fabrication process

2.2.1 Synthesis of Co_3O_4 nanoparticles

8.8 mL of NaOH solution (10 mol·L^{-1}) was gradually added into 40 mL of $CoCl_2$ solution (1 mol·L^{-1}) with a constant stirring at 400 r·min^{-1} for 15 min. Then, the pH value of the solution was adjusted to 7 using dropwise addition of 1 mol·L^{-1} HCl solution. The color of the solution changes from dark blue to light pink, indicating the formation of $Co(OH)_2$. The pink precipitates were then centrifuged and washed with water for three times. The obtained $Co(OH)_2$ was then transferred to a Labec Muffle furnace and calcinated at 450 °C for 6 h to produce a black Co_3O_4 NP powder.

2.2.2 Synthesis of PDA-coated Co_3O_4 NPs (Co_3O_4@PDA)

Co_3O_4@PDA NPs were subsequently prepared by self-polymerization of dopamine on the surfaces of the Co_3O_4 NPs. Briefly, 5 mL of Co_3O_4 NPs' suspension (200 mg·mL^{-1}) was dispersed into an aqueous solution of dopamine hydrochloride (2 mg·mL^{-1}) in tris buffer solution (pH = 8.5) with $CuSO_4$ (5×10^{-3} mol·L^{-1}) and H_2O_2 (19.6×10^{-3} mol·L^{-1}) with a constant stirring at 300 r·min^{-1} for 0.5 h. Subsequently, the obtained Co_3O_4@PDA particles were centrifuged and washed with water for three times. The sample was dried in vacuum overnight.

2.2.3 Fabrication photothermal aerogel sheets as 2D photothermal evaporators

An aliquot of either Co_3O_4 or Co_3O_4@PDA NP was initially dispersed into a mixture of water and ethanol

($V_{water}:V_{ethanol} = 7:1$) containing agarose (12.5 mg·mL^{-1}) and urea (0.125 g·mL^{-1}), which was continuously stirred at 85 °C for 30 min. Thereafter, 2 mL of the obtained suspension was dropped evenly on a piece of circular commercial cellulose–cotton sheet having a diameter of 2.6 cm. The obtained photothermal sheet was cooled naturally to room temperature and pre-frozen at -20 °C overnight followed by freeze drying. The resultant 2D photothermal aerogel sheets were designated as Co$_3$O$_4$-10, Co$_3$O$_4$-15, Co$_3$O$_4$-20, Co$_3$O$_4$-25, Co$_3$O$_4$@PDA-10, Co$_3$O$_4$@PDA-15, and Co$_3$O$_4$@PDA-20, where the number indicated the concentration (mg·mL^{-1}) of either Co$_3$O$_4$ or Co$_3$O$_4$@PDA NPs in the suspension. For preparation of the Co$_3$O$_4$@PDA-rGO photothermal aerogel, additional rGO nanosheets (0.2 or 0.4 mg·mL^{-1}) were added into the Co$_3$O$_4$@PDA suspension (15 mg·mL^{-1}). The obtained samples were designated as Co$_3$O$_4$@PDA-rGO-0.2 and Co$_3$O$_4$@PDA-rGO-0.4 photothermal aerogel, respectively.

2.2.4 Fabrication of 3D photothermal aerogel-based evaporators

A piece of 2D Co$_3$O$_4$@PDA-rGO-0.4 photothermal aerogel sheet (11 cm × 11 cm) was cut and wrapped on a polystyrene (PS) foam cylinder to form the 3D Co$_3$O$_4$@PDA-rGO photothermal aerogel-based evaporators with a consistent diameter of 2.6 cm and three different heights (2, 3 and 4 cm).

2.3 Characterization

Scanning electron microscopy (SEM) images were captured on a Zeiss Merlin scanning electron microscope. Transmission electron microscopy (TEM) images were obtained using a JEOL JEM 2100F transmission electron microscope. Light absorption capability of the photothermal aerogel was measured using a Shimadzu UV-2600 Spectrophotometer. The X-ray photoelectron spectroscopy (XPS) analysis was carried out on a Kratos Axis Ultra with a Delay Line Detector photoelectron spectrometer using an aluminum monochromatic X-ray source. Contact angle measurement was conducted on a Dataphysics OCA 20 contact angle system.

2.4 Solar-steam generation test

Solar-steam generation tests were conducted under controlled laboratory conditions (ambient temperature 25 °C and relative humidity 30%). The solar evaporation system was placed on an electronic balance which was connected to a computer to monitor mass loss in real time. A Newport Oriel Solar Simulator (class ABA, 450 W, Newport Oriel 69920) was used to provide simulated sunlight with an intensity of 1.0 kW·m^{-2}. An IR camera (FLIR E64501) was used to monitor the temperature of all evaporation surfaces. Seawater for desalination tests was collected at Semaphore

Beach in Adelaide, Australia. The concentrations of major ions in seawater and collected clean water were analyzed using an Inductively Coupled Plasma-Mass Spectrometry (ICP-MS) Triple Quad system (ICP-QQQ, Agilent 8800).

3 Results and discussion

The synthetic procedure for the Co$_3$O$_4$@PDA-rGO-based photothermal aerogel is shown in Fig. 2a. Initially, Co(OH)$_2$ was synthesized and calcinated to form Co$_3$O$_4$ NPs. Then, a PDA layer was coated on the surfaces of Co$_3$O$_4$ NP by self-polymerization of dopamine. The synthesized Co$_3$O$_4$@PDA NPs and rGO nanosheets were then dispersed in a hot agarose solution and cast onto a piece of cotton–cellulose sheet (CCS) followed by self-gelation to form the Co$_3$O$_4$@PDA-rGO-based photothermal aerogel sheet. The obtained photothermal aerogel sheet was either directly applied as 2D evaporator or utilized to fabricate 3D cylindrical evaporators (Fig. 2a). Figure S1 shows the X-ray diffraction (XRD) pattern of the synthesized Co$_3$O$_4$ NPs. All the diffraction peaks can be indexed to a cubic phase Co$_3$O$_4$ (JCPDS 43-1003). SEM images of the synthesized Co$_3$O$_4$ showed a particulate shape with sizes ranging from 38 to 70 nm (Fig. 2b). After PDA coating, the shape and size of the Co$_3$O$_4$@PDA NPs did not significantly change (Fig. 2c), implying that a very thin layer of PDA was grown on the surfaces of the Co$_3$O$_4$ NPs. High-resolution TEM image of the Co$_3$O$_4$@PDA NPs confirmed that the thickness of the amorphous PDA layer was only about 1.4 nm (Fig. 2d). The SEM image of the commercial rGO used showed the characteristic 2D nanosheet structure (Fig. S2). Element N was detected in the XPS survey spectrum of the Co$_3$O$_4$@PDA NPs (Fig. 2e), also confirming the formation of a PDA coating on the Co$_3$O$_4$ surface. High-resolution XPS spectrum (Fig. 2f) of Co 2p for the Co$_3$O$_4$@PDA NPs showed two characteristic peaks attributable to Co 2p$_{3/2}$ (778.4 eV) and Co 2p$_{1/2}$ (793.6 eV) [46]. The C 1 s peak observed for Co$_3$O$_4$@PDA NPs could be deconvoluted to C=O (288.6 eV), C–N/C–O (286.0 eV), and C–H (284.8 eV), corresponding to the major peaks expected for PDA (Fig. 2g) [34].

Commercial CCS served as a good substrate for the loading of photothermal materials because of its superhydrophilicity which favored water transportation during solar steam generation. As shown in Fig. S3a, b, due to strong capillary action, water could be quickly transported upward to reach a height of 6.4 cm within 60 s. In addition, the abundant surface structure of the CCS led to a relatively large surface area for light absorption and water evaporation. As shown in Fig. 3a, the top surface of the CCS was composed of both 1D and 2D structures. High-resolution SEM images revealed that the 1D fiber had a diameter of 9.7–17.8 μm (Fig. 3b), which was corresponded to cotton fiber components, while
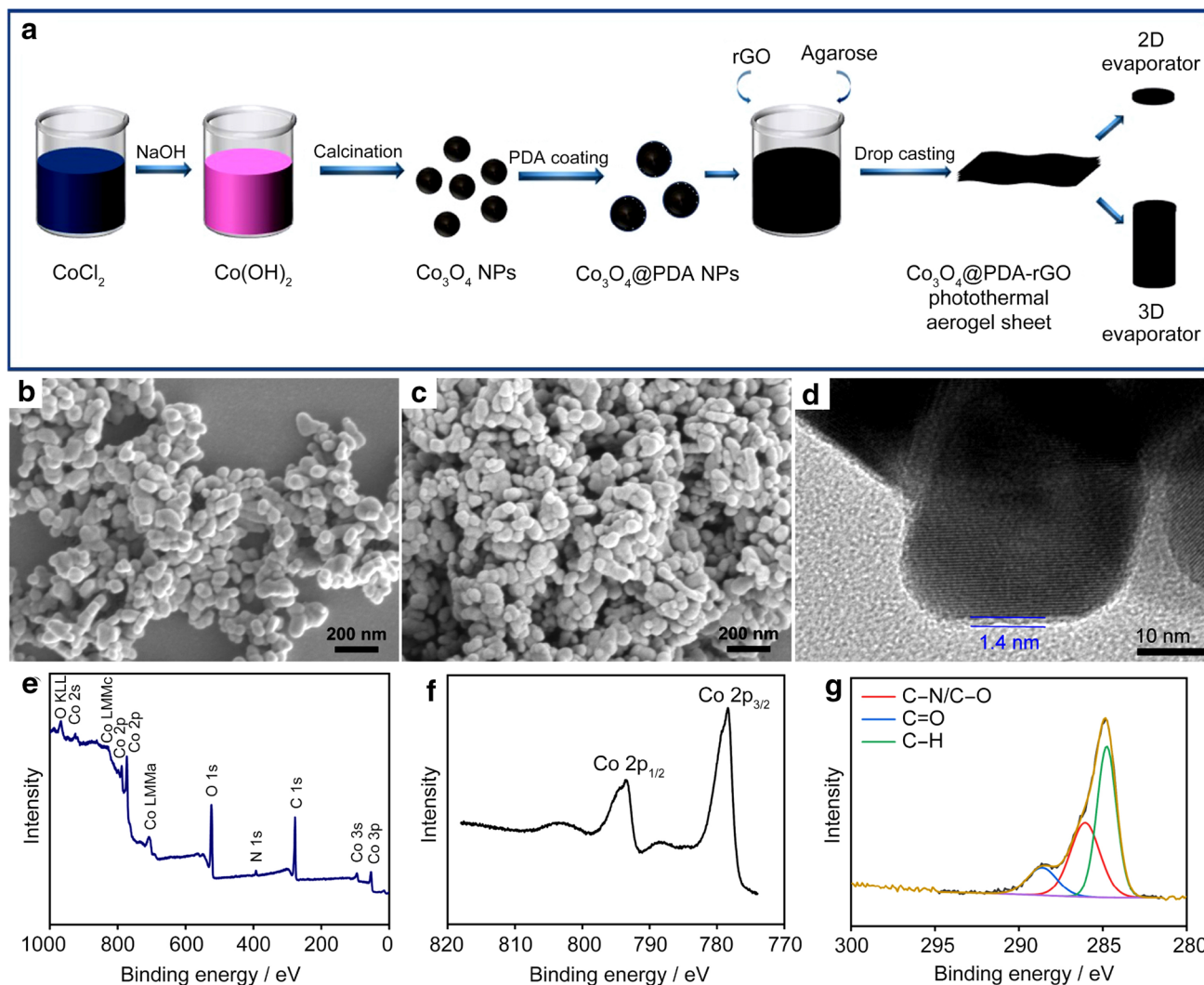
Fig. 2 a Schematic illustration of the fabrication process of the Co_3O_4@PDA-rGO-based photothermal aerogels. SEM images of **b** Co_3O_4 and **c** Co_3O_4@PDA NPs. **d** High-resolution TEM image of the Co_3O_4@PDA NPs. **e** XPS survey spectrum of the Co_3O_4@PDA NPs, and high-resolution XPS spectra of **f** Co 2p and **g** C 1s for the Co_3O_4@PDA NPs

the 2D film had more pores which were typical structures for a cellulose sponge (Fig. 3c). The cross-sectional SEM image of the CCS showed a multilayered structure (Fig. S4a). After drop-casting, the thickness of each layer increased (Fig. S4b). The top surface of the obtained Co_3O_4@PDA-rGO aerogel sheet was fully covered by a combination of Co_3O_4@PDA, rGO, and agarose (Fig. 3d). The interspace between the cotton fibers and the pores of the cellulose film were all filled with PTMs and agarose (Fig. 3e). Wrinkled agarose gel and Co_3O_4-PDA NPs were also observed distributed across the surface (Fig. 3f). Compared to the pristine CCS, the XPS survey spectrum of the Co_3O_4@PDA-rGO photothermal aerogel sheet indicated the additional presence of elemental Co from Co_3O_4@PDA NPs and significant increases in both elemental O and C, which was attributed to rGO, Co_3O_4@PDA and agarose (Fig. S5), confirming the

successful loading of PTMs on the CCS surface. Accordingly, the color of the pristine CCS changed from white to dark black (Fig. 3g). The Co_3O_4@PDA NPs and rGO nanosheets were firmly adhered to the surface of CCS by agarose, so that followed repeated strong finger abrasion, no black materials were detached from the aerogel sheet (Fig. S6). The photothermal aerogel sheet also displayed excellent mechanical strength. As shown in Fig. S7, a small piece of aerogel sheet (2.0 cm × 2.2 cm) could easily hold about 1.0 kg weight. The obtained Co_3O_4@PDA-rGO aerogel sheet was also hydrophilic due to the innate hydrophilicity of the CCS, agarose, and Co_3O_4@PDA NPs. As shown in Fig. S8, during contact angle measurement, a water droplet was quickly absorbed by the photothermal aerogel within 1.0 s. The water transportation ability of the photothermal aerogel sheet was slightly better than that of the pristine CCS. Water
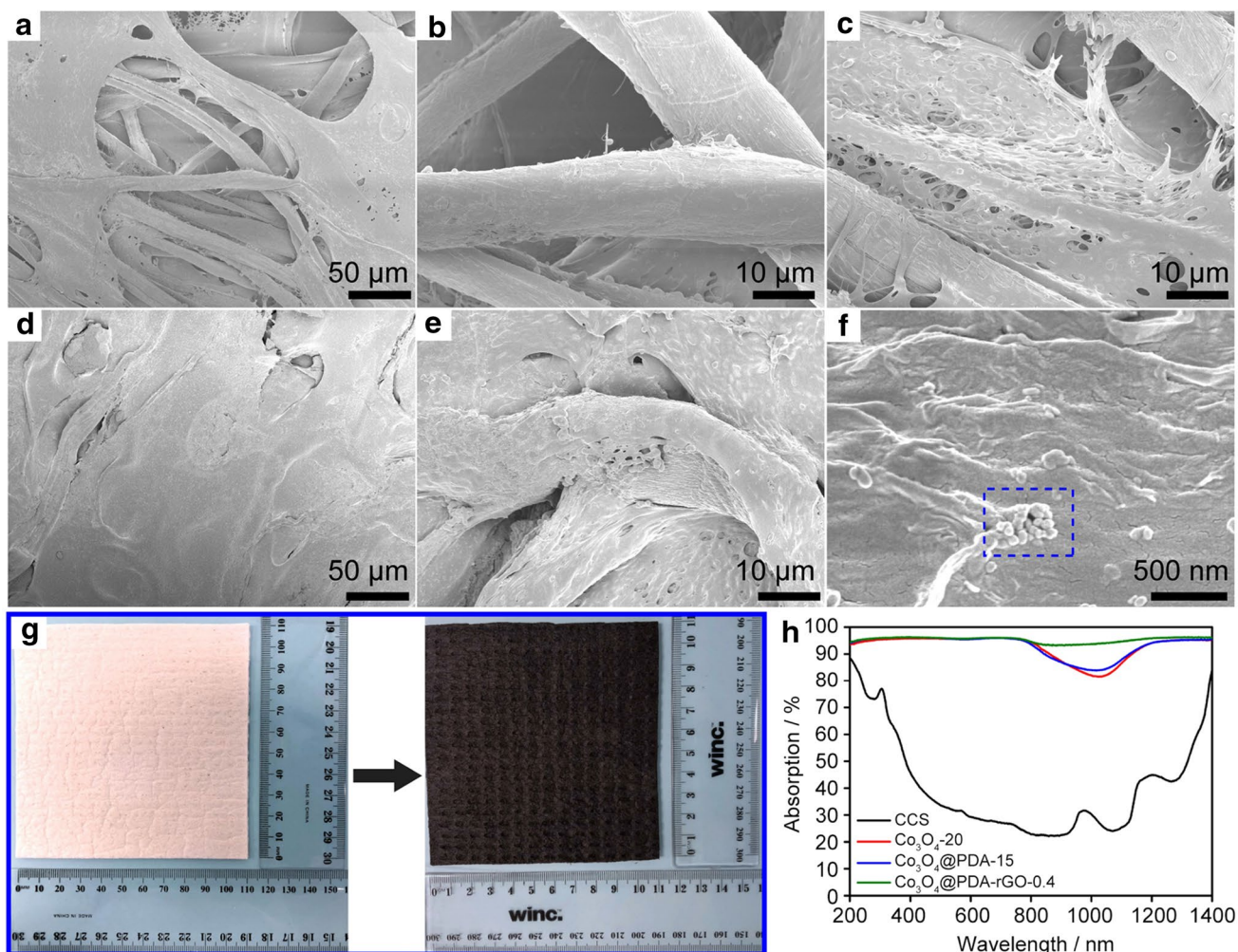
Fig. 3 SEM images of the top surface of **a–c** pristine CCS and **d–f** Co_3O_4@PDA-rGO photothermal aerogel sheet. **g** Photographs of CCS before and after drop-casting. **f** Light absorption of the pristine CCS, Co_3O_4-20, Co_3O_4@PDA-15, and Co_3O_4@PDA-rGO-0.4 aerogel sheets, respectively

could be quickly transported upward by 6.5 cm within 60 s (Fig. 3c, d). The solar absorbing capabilities of photothermal aerogels were measured to evaluate their light-to-heat conversion performance. As shown in Fig. 3h, the Co_3O_4@PDA-rGO aerogel sheet showed the strongest light absorption of 93.8–96.4% across the UV–Vis–NIR regions, which was better than that of the pristine CCS and the aerogels prepared using both Co_3O_4 and Co_3O_4@PDA NPs.

The evaporation performances of the fabricated photothermal aerogel-based evaporators were tested using an oil lamp-like design under 1.0 sun irradiation (Figs. 4a and S9). Initially, 2D photothermal aerogel sheets, prepared with different PTMs (Co_3O_4, Co_3O_4@PDA, and Co_3O_4@PDA-rGO), were investigated to identify the optimal material for subsequent experiments. For the Co_3O_4 NP-coated aerogel sheets, the evaporation rate increased with the Co_3O_4 NPs concentration (Fig. 4b). For example, when the concentration

of Co_3O_4 NPs was 10 mg·mL^{-1}, the evaporation rate of the Co_3O_4-10 aerogel sheet was 1.21 kg·m^{-2}·h^{-1}, but the evaporation rate increased to 1.28 kg·m^{-2}·h^{-1} (Co_3O_4-15) and 1.32 kg·m^{-2}·h^{-1} (Co_3O_4-20) when the NP concentration increased to 15 and 20 mg·mL^{-1}, respectively. Further increase in the concentration of Co_3O_4 NPs to 25 mg·mL^{-1} led to no additional increase in the evaporation rate. Using Co_3O_4@PDA NPs as PTMs could remarkably enhance solar steam generation. The evaporation rate of the aerogel prepared with 10, 15, and 20 mg·mL^{-1} of Co_3O_4@PDA NPs (Co_3O_4@PDA-10, Co_3O_4@PDA-15, and Co_3O_4@PDA-15) were 1.36, 1.51, and 1.51 kg·m^{-2}·h^{-1}, respectively, which were all higher than that of the Co_3O_4-20 aerogel prepared with 20 mg·mL^{-1} Co_3O_4 NPs (1.32 kg·m^{-2}·h^{-1}). Therefore, the optimized concentration of the used Co_3O_4@PDA was identified as 15 mg·mL^{-1}. When additional small amounts of rGO (0.2 or 0.4 mg·mL^{-1}) were added, the evaporation rates
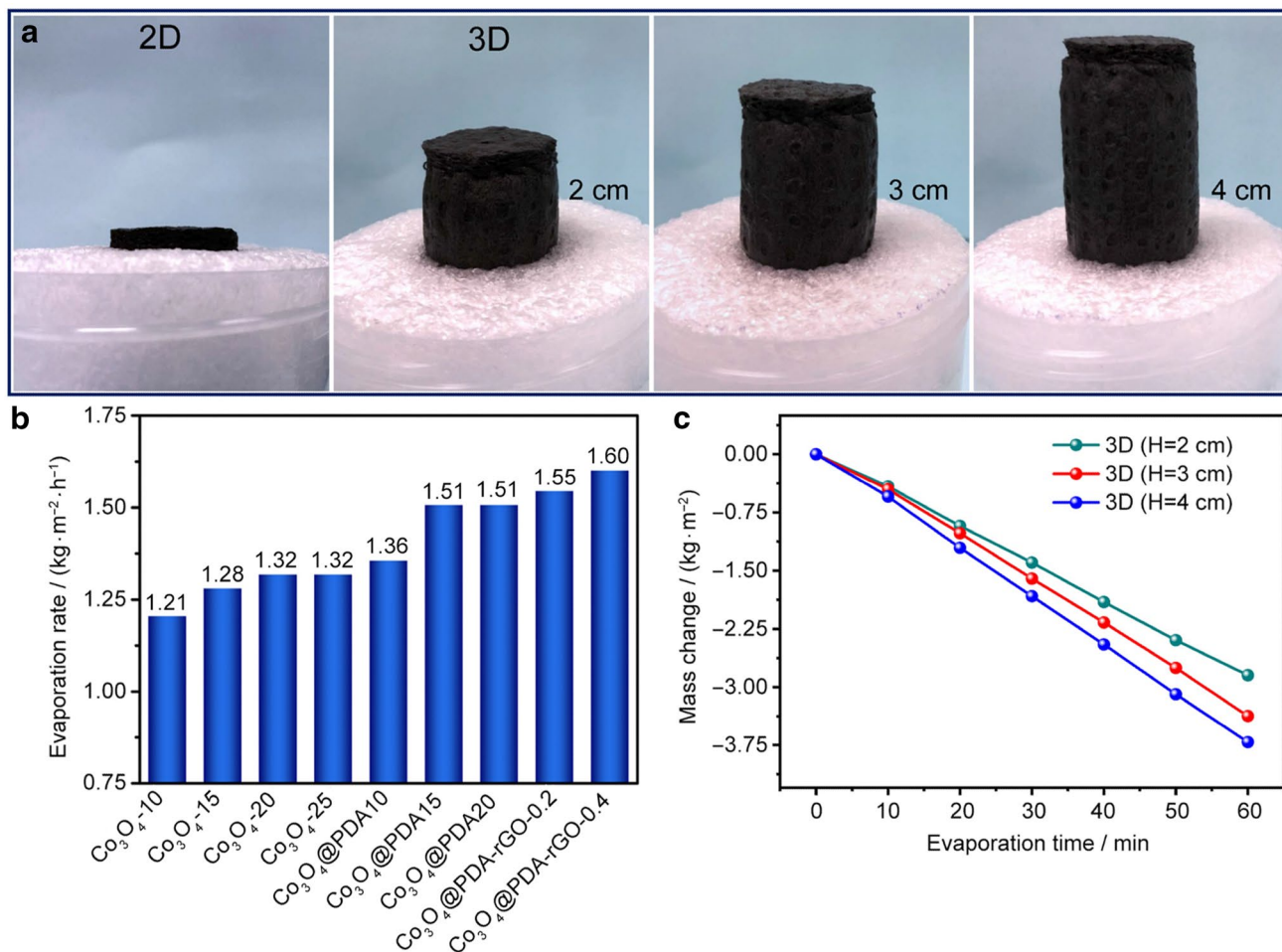
Fig. 4 **a** Digital photographs of the 2D Co_3O_4@PDA-rGO-0.4 aerogel with a diameter of 2.6 cm and the fabricated 3D cylindrical evaporators with heights of 2, 3, and 4 cm. **b** Evaporation rates of different 2D photothermal aerogels prepared with Co_3O_4, Co_3O_4@PDA, and rGO. **c** Mass changes of the 3D photothermal evaporators with different heights (2, 3, and 4 cm)

of the corresponding Co_3O_4@PDA-rGO-0.2 and Co_3O_4@PDA-rGO-0.4 photothermal aerogels were further increased to 1.55 and 1.60 $kg \cdot m^{-2} \cdot h^{-1}$, respectively (Fig. 4c). Therefore, the Co_3O_4@PDA-rGO-0.4 aerogel showed the best performance during solar steam generation which was then tailored to fabricate 3D cylindrical photothermal evaporators with heights of 2, 3, and 4 cm for further tests (Figs. 4a, and S10).

It has been proved that compared with the 2D photothermal evaporator, the 3D counterpart could offer more evaporation surface area and also introduce cold evaporation surfaces to harvest additional energy from the surrounding air, which significantly enhance solar steam generation. Herein, the Co_3O_4@PDA-rGO-0.4 aerogel-based 3D evaporators with heights of 2, 3, and 4 cm delivered extremely high evaporation rates of 2.85, 3.37, and 3.71 $kg \cdot m^{-2} \cdot h^{-1}$, respectively (Fig. 4c), which were much higher than that of the 2D Co_3O_4@PDA-rGO-0.4 photothermal aerogel (1.60 $kg \cdot m^{-2} \cdot h^{-1}$). The evaporation rate of the

4 cm-tall photothermal evaporator was higher than that of most recently reported 3D evaporators (Table S1). Theoretically, the evaporation rate would further increase with the increase in height of the 3D evaporator [17, 33]. For example, when the height of the 3D evaporator was increased from 4 to 6 cm, the evaporation rate was increased from 3.71 to 4.35 $kg \cdot m^{-2} \cdot h^{-1}$ (Fig. S11a). However, to achieve such a 17% increment in the evaporation rate, the material consumption was increased by 43% (Fig. S11b). Therefore, considering the balance between the evaporation rate and material cost, the 4 cm-tall 3D evaporator was selected for further study.

The light-to-vapor energy conversion efficiency (η) for solar steam generation was estimated using the following equations (Eqs. 1–3):

$$\eta = \frac{m(H_{LV} + Q)}{E_{in}} \tag{1}$$

$$H_{LV} = 1.91846 \times 10^6 [T_1/(T_1 - 33.91)]^2 \quad (2)$$

$$Q = c(T_1 - T_0,), \quad (3)$$

where m is the net water evaporation rate (with dark evaporation rate deducted, 0.38 kg·m^{-2}·h^{-1} for 2D aerogel and 2.16 kg·m^{-2}·h^{-1} for 4 cm-tall 3D evaporator), H_{LV} is the latent heat required for vaporization of water (J·kg^{-1}), T_1 is the stable evaporation temperature of the top evaporation surface (K), Q is the heat for increasing water temperature on evaporation surface (J·kg^{-1}), c is the specific heat of water (4.2 J·g^{-1}·K^{-1}), T_0 is the initial temperature of the top surface before solar evaporation (K), and E_{in} (kJ·m^{-2}·h^{-1}) is the energy input of the incident light (1.0 kw·m^{-2}). According to the above equations, η of the 2D Co$_3$O$_4$@PDA-rGO-0.4 photothermal aerogel was calculated to be 84%, while η of the 3D evaporator (4 cm tall) was 107%, exceeding the theoretical limit.

To explain the extremely high energy efficiency of the 3D photothermal evaporator (4 cm tall), the energy exchange between the evaporation surfaces and surrounding environment was calculated according to following equation (Eq. (4)):

$$E_{environment} = -A_1 \varepsilon \sigma (T_1^4 - T_E^4) - A_2 \varepsilon \sigma (T_2^4 - T_E^4) \\ - A_1 h(T_1 - T_E) - A_2 h(T_2 - T_E), \quad (4)$$

where A_1 is the area of top evaporation surface, A_2 is the side evaporation surface area, T_E is the ambient temperature (K), ε is emissivity of the evaporation surface (~ 0.90), σ is the Stefan–Boltzmann constant (5.67×10^{-8} W·m^{-2}·K^{-4}), and h is convection heat transfer coefficient (10 W·m^{-2}·K^{-1}). During solar evaporation, for the 2D photothermal aerogel (Fig. 5a–e), the stable average temperature was around 30.9 °C, which was significantly higher than the ambient temperature (25 °C). The calculated energy loss by convection and radiation from the top evaporation surface to the surrounding environment was about 0.05 W. For the 3D photothermal evaporator, the side surface served as cold evaporation surfaces which could draw energy from the top evaporation surface, thus lowering the temperature and consequent energy loss thereof [17, 33]. The measured steady temperature of the top evaporation surface of the 3D evaporator was only 26.2 °C (Fig. 5f–j), which was much lower than that of the 2D aerogel (30.9 °C). The temperature of the top evaporation surface was only slightly higher than the ambient temperature (25 °C). Therefore, the calculated energy loss from the top evaporation surface to the environment was only 0.01 W. The average surface temperature of the side surface of the 3D evaporator was only 18.4 °C (Fig. 5f–j), which was much lower than the environmental temperature, thus harvesting energy from the environment (0.33 W). Therefore, the 3D evaporator achieved a net energy gain of 0.32 W from the environment, which led to
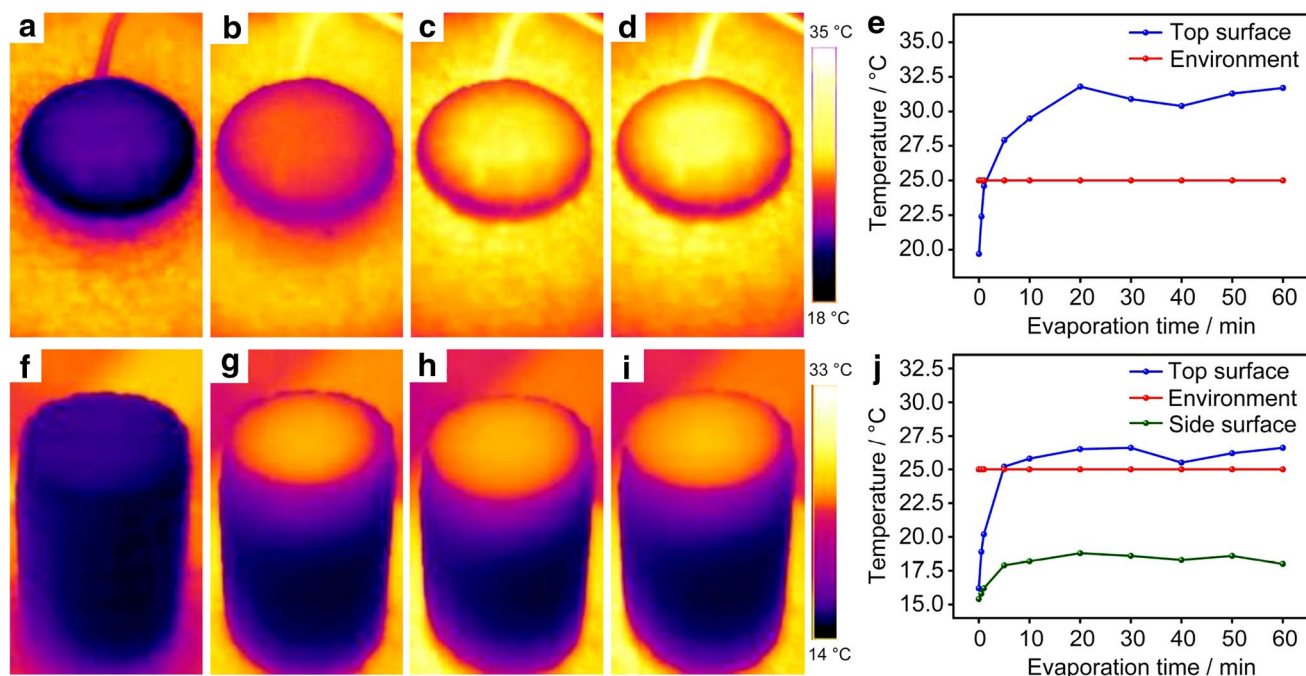

Fig. 5 IR images of the 2D aerogel evaporator under 1.0 sun irradiation for **a** 0, **b** 1, **c** 5, and **d** 30 min, and **e** the time-dependent temperature curve of the evaporation surface. IR images of the 3D evaporator with a height of 4.0 cm under 1.0 sun irradiation for **f** 0, **g** 1, **h** 5, and **i** 30 min, and **j** the time-dependent temperature curve of the top and side evaporation surfaces
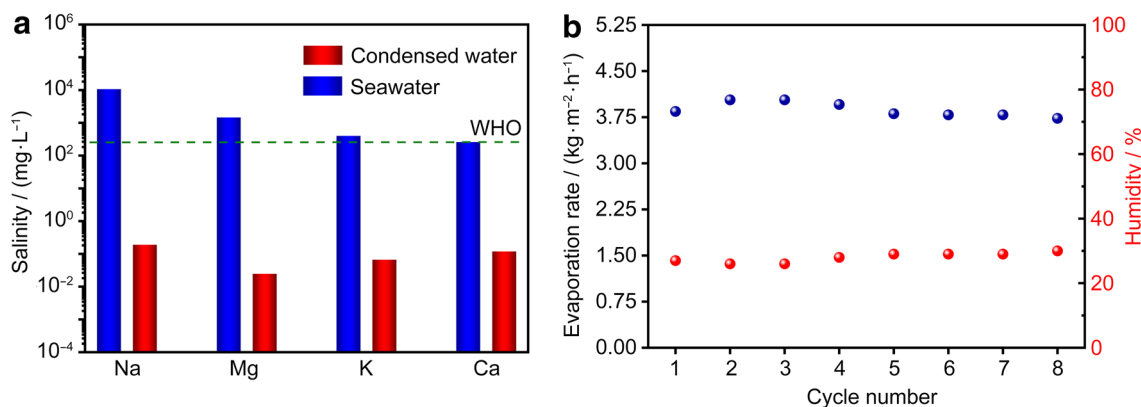
Fig. 6 **a** Concentrations of the major irons in the original seawater and condensed water collected during solar steam generation. **b** Stability test for the 3D evaporator with a height of 4.0 cm under 1.0 sun irradiation for eight cycles

an extremely high evaporation rate and an energy conversion efficiency beyond the theoretical limit.

To evaluate the feasibility of using the Co_3O_4@PDA-rGO aerogel-based 3D evaporator (4 cm tall) for desalination, solar evaporation of real seawater under 1.0 sun was investigated. ICP-MS was utilized to test and compare the concentrations of the major ions of Na^+, K^+, Ca^{2+}, Mg^{2+} in seawater and the condensed water collected during solar evaporation. As shown in Fig. 6a, the concentrations of Na^+, K^+, Ca^{2+}, Mg^{2+} in the condensed water were dramatically lowered to 0.19, 0.07, 0.12, and 0.02 mg·L^{-1}, respectively which were well below the salinity level of drinkable desalinated water defined by World Health Organization (WHO) [61]. Co ions were not detected in both condensed water and residual seawater, confirming the excellent chemical stability of Co_3O_4 against seawater. Cycling evaporation tests under 1.0 sun were also performed to assess the stability of the Co_3O_4@PDA-rGO aerogel-based 3D evaporator during repeated seawater desalination. The evaporation rates over eight cycles (1 h per cycle) remained relatively constant within the range of 3.73 to 4.03 kg·m^{-2}·h^{-1}. The slight variation in evaporation rate was due to the fluctuation of the ambient humidity (26–29%) [19, 51]. The overall average seawater evaporation rate was 3.87 kg·m^{-2}·h^{-1} which was slightly higher than that of the pure water evaporation due to the lower ambient humidity [19, 51]. The 3D evaporator also showed good salt resistance properties. As shown in Fig. S12, after 1 h seawater desalination test, no salt crystals were observed on either the top or side evaporation surfaces.

4 Conclusion

In summary, Co_3O_4@PDA NPs were synthesized and utilized together with rGO nanosheets to prepare new Co_3O_4@PDA-rGO photothermal aerogel sheets. The obtained

photothermal aerogel sheet could be tailored to fabricate both 2D flat and 3D cylindrical evaporators. Due to the strong light absorption and superhydrophilicity, both the obtained 2D and 3D evaporators showed excellent performance during solar steam generation. The evaporation rate of the 2D aerogel was 1.60 kg·m^{-2}·h^{-1}, with a corresponding energy efficiency of 84%. While for the 3D evaporator (4 cm high), due to the enlarged evaporation surface area, decreased energy loss from top evaporation surface to the environment, and the energy gain on the side evaporation surface from the environment, the evaporation rate was dramatically increased to 3.71 kg·m^{-2}·h^{-1}, with a light-to-vapor energy efficiency of 107%. The Co_3O_4@PDA-rGO photothermal aerogel-based 3D evaporator also showed excellent performance and stability during continuous seawater desalination, where the concentration of Na^+ in the collected condensed water was only 0.19 mg·L^{-1}. Thus, the Co_3O_4@PDA-rGO aerogel-based evaporators are promising for practical applications.

References

1. Wu X, Chen GY, Owens G, Chu D, Xu H. Photothermal materials: a key platform enabling highly efficient water evaporation driven by solar energy. Mater Today Energy. 2019;12:277.
2. Liu H, Huang Z, Liu K, Hu X, Zhou J. Interfacial solar-to-heat conversion for desalination. Adv Energy Mater. 2019;9(21):1900310.
3. Wang P. Emerging investigator series: the rise of nano-enabled photothermal materials for water evaporation and clean water production by sunlight. Environ Sci Nano. 2018;5(5):1078.
4. Li J, Du M, Lv G, Zhou L, Li X, Bertoluzzi L, Liu C, Zhu S, Zhu J. Interfacial solar steam generation enables fast-responsive, energy-efficient, and low-cost off-grid sterilization. Adv Mater. 2018;30(49):1805159.

5. Zhu L, Gao M, Peh CKN, Ho GW. Recent progress in solar-driven interfacial water evaporation: advanced designs and applications. Nano Energy. 2019;57:507.

6. Tao P, Ni G, Song C, Shang W, Wu J, Zhu J, Chen G, Deng T. Solar-driven interfacial evaporation. Nat Energy. 2018;3(12):1031.

7. Zhou L, Li X, Ni GW, Zhu S, Zhu J. The revival of thermal utilization from the Sun: interfacial solar vapor generation. Natl Sci Rev. 2019;6(3):562.

8. Zhou Y, Ding T, Gao M, Chan KH, Cheng Y, He J, Ho GW. Controlled heterogeneous water distribution and evaporation towards enhanced photothermal water-electricity-hydrogen production. Nano Energy. 2020;77:105102.

9. Meng FL, Gao M, Ding T, Yilmaz G, Ong WL, Ho GW. Modular deformable steam electricity cogeneration system with photothermal, water, and electrochemical tunable multilayers. Adv Funct Mater. 2020;30(32):2002867.

10. Gao M, Peh CK, Zhu L, Yilmaz G, Ho GW. Photothermal catalytic gel featuring spectral and thermal management for parallel freshwater and hydrogen production. Adv Energy Mater. 2020;10(23):2000925.

11. Zhang P, Liao Q, Yao H, Huang Y, Cheng H, Qu L. Direct solar steam generation system for clean water production. Energy Storage Mater. 2019;18:429.

12. Gao MM, Zhu LL, Peh CK, Ho GW. Solar absorber material and system designs for photothermal water vaporization towards clean water and energy production. Energy Environ Sci. 2019;12(3):841.

13. Ghasemi H, Ni G, Marconnet AM, Loomis J, Yerci S, Miljkovic N, Chen G. Solar steam generation by heat localization. Nat Commun. 2014;5:4449.

14. Zeng Y, Yao J, Horri BA, Wang K, Wu Y, Li D, Wang H. Solar evaporation enhancement using floating light-absorbing magnetic particles. Energy Environ Sci. 2011;4(10):4074.

15. Zhang LB, Tang B, Wu JB, Li RY, Wang P. Hydrophobic light-to-heat conversion membranes with self-healing ability for interfacial solar heating. Adv Mater. 2015;27(33):4889.

16. Wang Y, Wu X, Shao B, Yang X, Owens G, Xu H. Boosting solar steam generation by structure enhanced energy management. Sci Bull. 2020;65(16):1380.

17. Storer DP, Phelps JL, Wu X, Owens G, Khan NI, Xu H. Graphene and rice-straw-fiber-based 3D photothermal aerogels for highly efficient solar evaporation. ACS Appl Mater Interfaces. 2020;12(13):15279.

18. Lu Y, Wang X, Fan D, Yang H, Xu H, Min H, Yang X. Biomass derived Janus solar evaporator for synergic water evaporation and purification. Sustain Mater Technol. 2020;25:e00180.

19. Wu X, Gao T, Han C, Xu J, Owens G, Xu HA. photothermal reservoir for highly efficient solar steam generation without bulk water. Sci Bull. 2019;64(21):1625.

20. Yang T, Lin H, Lin KT, Jia B. Carbon-based absorbers for solar evaporation: steam generation and beyond. Sustain Mater Technol. 2020;25:e00182.

21. Zhang P, Li J, Lv L, Zhao Y, Qu L. Vertically aligned graphene sheets membrane for highly efficient solar thermal generation of clean water. ACS Nano. 2017;11(5):5087.

22. Chen Y, Shi Y, Kou H, Liu D, Huang Y, Chen Z, Zhang B. Self-floating carbonized tissue membrane derived from commercial facial tissue for highly efficient solar steam generation. ACS Sustain Chem Eng. 2019;7(3):2911.

23. Zhu L, Gao M, Peh CK, Wang X, Ho GW. Self-contained monolithic carbon sponges for solar-driven interfacial water evaporation distillation and electricity generation. Adv Energy Mater. 2018;8(16):1702149.

24. Hu X, Xu W, Zhou L, Tan Y, Wang Y, Zhu S, Zhu J. Tailoring graphene oxide-based aerogels for efficient solar steam generation under one sun. Adv Mater. 2017;29(5):1604031.

25. Xu N, Hu XZ, Xu WC, Li XQ, Zhou L, Zhu SN, Zhu J. Mushrooms as efficient solar steam-generation devices. Adv Mater. 2017;29(28):1606762.

26. Deng Z, Miao L, Liu PF, Zhou J, Wang P, Gu Y, Wang X, Cai H, Sun L, Tanemura S. Extremely high water-production created by a nanoink-stained PVA evaporator with embossment structure. Nano Energy. 2019;55:368.

27. Gong F, Li H, Wang W, Huang J, Xia D, Liao J, Wu M, Papavassiliou DV. Scalable, eco-friendly and ultrafast solar steam generators based on one-step melamine-derived carbon sponges toward water purification. Nano Energy. 2019;58:322.

28. Gao M, Peh CK, Phan HT, Zhu L, Ho GW. Solar absorber gel: localized macro-nano heat channeling for efficient plasmonic au nanoflowers photothermic vaporization and triboelectric generation. Adv Energy Mater. 2018;8(25):1800711.

29. Zhu M, Li Y, Chen F, Zhu X, Dai J, Li Y, Yang Z, Yan X, Song J, Wang Y, Hitz E, Luo W, Lu M, Yang B, Hu L. Plasmonic wood for high-efficiency solar steam generation. Adv Energy Mater. 2018;8(4):1701028.

30. Liu Y, Yu S, Feng R, Bernard A, Liu Y, Zhang Y, Duan H, Shang W, Tao P, Song C, Deng TA. Bioinspired, reusable, paper-based system for high-performance large-scale evaporation. Adv Mater. 2015;27(17):2768.

31. Chen C, Zhou L, Yu J, Wang Y, Nie S, Zhu S, Zhu J. Dual functional asymmetric plasmonic structures for solar water purification and pollution detection. Nano Energy. 2018;51:451.

32. Wang H, Miao L, Tanemura S. Morphology control of Ag polyhedron nanoparticles for cost-effective and fast solar steam generation. Solar RRL. 2017;1(3–4):1600023.

33. Shao B, Wang Y, Wu X, Lu Y, Yang X, Chen GY, Owens G, Xu H. Stackable nickel–cobalt@polydopamine nanosheet based photothermal sponges for highly efficient solar steam generation. J Mater Chem A. 2020;8(23):11665.

34. Wu X, Wu L, Tan J, Chen GY, Owens G, Xu H. Evaporation above a bulk water surface using an oil lamp inspired highly efficient solar-steam generation strategy. J Mater Chem A. 2018;6(26):12267.

35. Chen QM, Pei ZQ, Xu YS, Li Z, Yang Y, Wei Y, Ji Y. A durable monolithic polymer foam for efficient solar steam generation. Chem Sci. 2018;9(3):623.

36. Wu X, Chen GY, Zhang W, Liu X, Xu HA. Plant-transpiration-process-inspired strategy for highly efficient solar evaporation. Adv Sustain Syst. 2017;1(6):1700046.

37. Wang J, Li Y, Deng L, Wei N, Weng Y, Dong S, Qi D, Qiu J, Chen X, Wu T. High-performance photothermal conversion of narrow-bandgap Ti_2O_3 nanoparticles. Adv Mater. 2017;29(3):1603730.

38. Zhu L, Sun L, Zhang H, Yu D, Aslan H, Zhao J, Li Z, Yu M, Besenbacher F, Sun Y. Dual-phase molybdenum nitride nanorambutans for solar steam generation under one sun illumination. Nano Energy. 2019;57:842.

39. Wu X, Robson ME, Phelps JL, Tan JS, Shao B, Owens G, Xu H. A flexible photothermal cotton-CuS nanocage-agarose aerogel towards portable solar steam generation. Nano Energy. 2019;56:708.

40. Song C, Li T, Guo W, Gao Y, Yang C, Zhang Q, An D, Huang W, Yan M, Guo C. Hydrophobic $Cu_{12}Sb_4S_{13}$-deposited photothermal film for interfacial water evaporation and thermal antibacterial activity. New J Chem. 2018;42(5):3175.

41. Chen R, Wu Z, Zhang T, Yu T, Ye M. Magnetically recyclable self-assembled thin films for highly efficient water evaporation by interfacial solar heating. RSC Adv. 2017;7(32):19849.

42. Ding D, Huang W, Song C, Yan M, Guo C, Liu S. Non-stoichiometric $MoO_{3−x}$ quantum dots as a light-harvesting material for interfacial water evaporation. Chem Commun. 2017;53(50):6744.

43. Wu X, Xu J, Chen GY, Fan R, Liu X, Xu H. Harvesting, sensing and regulating light based on photo-thermal effect of Cu@CuO mesh. Green Energy Environ. 2017;2(4):387.

44. Xu J, Li X, Wu X, Wang W, Fan R, Liu X, Xu H. Hierarchical CuO colloidosomes and their structure enhanced photothermal catalytic activity. J Phys Chem C. 2016;120(23):12666.

45. Moon J, Kim TK, VanSaders B, Choi C, Liu Z, Jin S, Chen R. Black oxide nanoparticles as durable solar absorbing material for high-temperature concentrating solar power system. Sol Energy Mater Sol Cells. 2015;134:417.

46. Wang P, Gu Y, Miao L, Zhou J, Su H, Wei A, Mu X, Tian Y, Shi J, Cai H. Co_3O_4 nanoforest/Ni foam as the interface heating sheet for the efficient solar-driven water evaporation under one sun. Sustain Mater Technol. 2019;20:e00106.

47. Lu Y, Fan D, Xu H, Min H, Lu C, Lin Z, Yang X. Implementing hybrid energy harvesting in 3D spherical evaporator for solar steam generation and synergic water purification. Solar RRL. 2020;4:2000232.

48. Li J, Wang X, Lin Z, Xu N, Li X, Liang J, Zhao W, Lin R, Zhu B, Liu G, Zhou L, Zhu S, Zhu J. Over 10 kg m^{-2} h^{-1} evaporation rate enabled by a 3D interconnected porous carbon foam. Joule. 2020;4(4):928.

49. Li X, Li J, Lu J, Xu N, Chen C, Min X, Zhu B, Li H, Zhou L, Zhu S, Zhang T, Zhu J. Enhancement of interfacial solar vapor generation by environmental energy. Joule. 2018;2(7):1331.

50. Shi Y, Li R, Jin Y, Zhuo S, Shi L, Chang J, Hong S, Ng KC, Wang PA. 3D photothermal structure toward improved energy efficiency in solar steam generation. Joule. 2018;2(6):1171.

51. Song H, Liu Y, Liu Z, Singer MH, Li C, Cheney AR, Ji D, Zhou L, Zhang N, Zeng X, Bei Z, Yu Z, Jiang S, Gan Q. Cold vapor generation beyond the input solar energy limit. Adv Sci. 2018;5(8):1800222.

52. Li X, Lin R, Ni G, Xu N, Hu X, Zhu B, Lv G, Li J, Zhu S, Zhu J. Three-dimensional artificial transpiration for efficient solar waste-water treatment. Natl Sci Rev. 2018;5(1):70.

53. Li X, Xu W, Tang M, Zhou L, Zhu B, Zhu S, Zhu J. Graphene oxide-based efficient and scalable solar desalination under one sun with a confined 2D water path. Proc Natl Acad Sci. 2016;113(49):13953.

54. Liu PF, Miao L, Deng Z, Zhou J, Su H, Sun L, Tanemura S, Cao W, Jiang F, Zhao LD. A mimetic transpiration system for record high conversion efficiency in solar steam generator under one-sun. Mater Today Energy. 2018;8:166.

55. Zhou J, Gu Y, Liu P, Wang P, Miao L, Liu J, Wei A, Mu X, Li J, Zhu J. Development and evolution of the system structure for highly efficient solar steam generation from zero to three dimensions. Adv Funct Mater. 2019;29(50):1903255.

56. Wang W, Shi Y, Zhang C, Hong S, Shi L, Chang J, Li R, Jin Y, Ong C, Zhuo S, Wang P. Simultaneous production of fresh water and electricity via multistage solar photovoltaic membrane distillation. Nat Commun. 2019;10(1):3012.

57. Xue G, Chen Q, Lin S, Duan J, Yang P, Liu K, Li J, Zhou J. Highly efficient water harvesting with optimized solar thermal membrane distillation device. Global Chall. 2018;2(5–6):1800001.

58. Wang Y, Wu X, Yang X, Owens G, Xu H. Reversing heat conduction loss: extracting energy from bulk water to enhance solar steam generation. Nano Energy. 2020;78:105269.

59. Xu HL, Liu XK, Su G, Zhang B, Wang DY. Electrostatic repulsion-controlled formation of polydopamine-gold janus particles. Langmuir. 2012;28(36):13060.

60. Xu HL, Liu XK, Wang DY. Interfacial basicity-guided formation of polydopamine hollow capsules in pristine O/W emulsions—wtoward understanding of emulsion template roles. Chem Mater. 2011;23(23):5105.

61. Zhou L, Tan Y, Wang J, Xu W, Yuan Y, Cai W, Zhu S, Zhu J. 3D self-assembly of aluminium nanoparticles for plasmon-enhanced solar desalination. Nat Photon. 2016;10:393.

Dr. Hao-Lan Xu is a Senior Research Fellow at Future Industries Institute, the University of South Australia. He obtained his Ph.D. degree at Shanghai Institute of Ceramics, Chinese Academy of Sciences in 2008. Then, he worked at Max Planck Institute of Colloids and Interfaces as an Alexander von Humboldt Postdoctoral Fellow. He joined The University of South Australia in January 2011. His research interests include colloid and interface physical chemistry, catalysis, and solar-thermal energy conversion and applications.